A Novel Approach to Remote Detection in Medical Radar Applications Using Flexible Transmit Array Lenses

Rifa Atul Izza Asyari ⬛ , *Student Member, IEEE*, Kuan-Yuan Lee ⬛ , *Student Member, IEEE*,
Rezki El Arif ⬛ *, Member, IEEE*, Tzyy-Sheng Jason Horng ⬛ *, Fellow, IEEE*, and Daniel Teichmann ⬛ *, Member, IEEE*

Abstract—This study introduces a novel method employing adaptable transmitarray lenses for medical radar systems, enhancing the direction of electromagnetic beams in the far-field. The newly developed antenna array exhibited marked improvements in gain, bandwidth, return loss, and isolation within specific frequency ranges during testing. Comprehensive evaluations, including various focal lengths and bending scenarios, underscored the superior performance of this adaptable lens over prior techniques. Its exceptional precision and sensitivity render it an ideal tool for real-time remote health monitoring systems, particularly in pulse detection. The research findings consistently aligned the heart rates detected by this innovative method with standard reference rates, reaffirming its reliability and accuracy. This consistency highlights the potential of the transmitarray lenses as a valuable advancement in medical radar systems. The study not only validates the effectiveness and reliability of the lenses but also lays a solid foundation for further research and development in this field. The insights garnered are expected to significantly bolster the progression of radar technologies in healthcare, leading to more accurate, efficient, and non-invasive health monitoring solutions, thereby enhancing patient care and outcomes.

Index Terms—Metasurface, SIL radar, flexible transmitarray lens, healthcare radar.

I. INTRODUCTION

MONITORING vital signs consistently plays a critical role in promptly identifying heart rate variability (HRV), which holds clinical significance when diagnosing cardiovascular conditions. Traditional non-invasive contact devices

Rifa Atul Izza Asyari and Daniel Teichmann are with SDU Health Informatics and Technology, The Maersk Mc-Kinney Moller Institute, University of Southern Denmark, 5230 Odense, Denmark (e-mail: raia@mmmi.sdu.dk; date@mmmi.sdu.dk).
Kuan-Yuan Lee and Tzyy-Sheng Jason Horng are with the Department of Electrical Engineering, National Sun Yat-Sen University, Kaohsiung 804, Taiwan (e-mail: gavin@g-mail.nsysu.edu.tw; jason@ee.nsysu.edu.tw).
Rezki El Arif is with the Department of Biomedical Engineering, Institut Teknologi Sepuluh Nopember, Surabaya 60111, Indonesia (e-mail: rezki.arif@its.ac.id).
Digital Object Identifier 10.1109/JERM.2023.3347395

such as phonocardiogram (PCG) [1], photoplethysmograph (PPG) [2], ultrasound cardiography (UCG) [3], electrocardiography (ECG) [4] and impedance cardiography (ICG) [5] are commonly used for this purpose. However, these devices require direct skin contact, which causes discomfort and inconvenience for users. The integration of electromagnetic sensors into wearable devices offers the opportunity to revolutionize health monitoring by allowing continuous and non-invasive monitoring of biological information such as blood pressure, respiratory rate, and heart rate to be monitored non-invasively [6].

In recent years, wearable radar systems that use different approaches, such as ultra-wideband (UWB) [7], frequency modulated continuous wave (FMCW) [8], continuous wave [9], and self-injection locking (SIL) [10]-[17], have been proposed for physiological information detection. SIL-based radars offer inherent advantages in mitigating internal reflection and antenna transmit-receive coupling clutter [18], making them well-suited for integration into wearable devices. However, the duration of operation for such wearables is heavily dependent on the battery capacity. An alternative approach involves the use of passive nonlinear tags [19], such as harmonic-type tags [20] or intermodulation-type tags [21]. The efficiency of these devices is significant even when equipped with one antenna [22]. Nonetheless, the harmonic-tag necessitates dual-band operation of its antenna, while the intermodulation-type tag's transponder [23] necessitates high-selectivity diplexers, both presenting challenges in design and integration. Another technique involves leveraging RFID tags [24], [25] for heartbeat monitoring, but requires close proximity between the sensor reader and the tag; also in [26] it does not explain in detail the information about heart rate monitoring in longer terms.

In the realm of vital sign monitoring, traditional noninvasive contact devices require direct skin contact, often leading to user discomfort [27]. Recent wearable radar systems, although promising, grapple with issues ranging from battery longevity to design and integration complexities. The use of rigid materials [28] in previous work not only causes discomfort during extended use, but can also compromise the accuracy and reliability of the collected data. To overcome this, our research implements innovative non-contact techniques using adaptable transmitarray lenses, significantly reducing discomfort by eliminating the need for prolonged skin contact. This approach is supported by
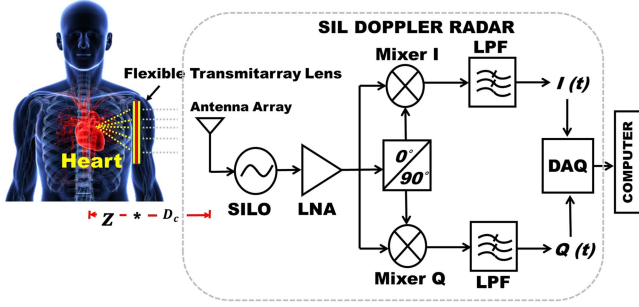
Fig. 1. Schematic representation of heart rate detection technique with a flexible TA lens and a remote SIL radar.

evidence such as the study [29] that highlights the importance of patient comfort in the design of medical technology. Moreover, the research detailed in [30] comprehensively explores the progress in noninvasive, flexible wearable medical technologies with a patient-centric approach. It highlights that a majority of the devices discussed in the study are made using materials that are flexible, stretchable, and lightweight, specifically chosen for the fabrication of biosensors.

To overcome these limitations, our study explores the potential of a flexible transmitarray lens to monitor vital signs using SIL radar technology at 5.8 GHz. The lens serves to focus the beam of the transmitter antenna through the human heart [31]. Experimental tests have been conducted to assess the stability of the lens in both flat and bent positions. Additionally, we have incorporated simulated skin and muscle layers to assess lens performance under realistic conditions. Our findings demonstrate that the use of flexible transmitarray lenses can overcome the limitations associated with rigid materials and wearable radar devices. Utilizing flexible substrates allows wearable devices to achieve more comfortable and precise heart rate monitoring. This research marks a significant step forward in enhancing the user experience and accuracy of health monitoring devices, making them more convenient, low-cost and efficient for daily use, even over extended periods, without the need for direct skin contact. It is important to note a drawback, namely the relatively large structure of these devices. However, we intend to address and improve this aspect in our future research endeavors.

This paper is systematized as follows. Section II presents a summary of the system architecture and its operating principles. Section III focuses on designing a multi-band radar antenna. Section IV introduces the design and investigation of the flexible transmitarray lens. Section V describes the setup for monitoring vital signs and presents the results. Finally, Section VI is the conclusion.

II. SIL RADAR STRUCTURE AND OPERATING PRINCIPLE

The radar system, as schematically depicted in Fig. 1, is an innovative assembly designed to operate at a frequency of 5.8 GHz [19]. Within this system, an individual wears a flexible transmit array carefully positioned near their aorta on the chest. On the opposite side of the individual stands the self-injection locking radar (SIL) [14], stationed at a strategic location to ensure optimal reception and transmission of signals. The radar's

core functionality revolves around a delay line frequency demodulator. This demodulator is tasked with interpreting the transmitted signals emanating from the Self-Injection Locking Oscillator (SILO). During this demodulation phase, the system is adept at extracting pivotal information: the Doppler phase shift, a consequence of the natural movement of the physiological activities. This phase shift becomes the precursor for the derivation of the heartbeat signal, a vital metric that offers information on real-time physiological responses, especially during physical exertion.

This adaptable lens, once incorporated, precisely focuses signals emitted by the SIL radar. Furthermore, it can relay the Doppler-shifted echo signals back to the SILO, enhancing the system's accuracy and efficiency.

$$S_{\text{SILO}}(t) = A_{\text{SILO}} \cos\left(\omega_{\text{SILO}}\, t + (\Delta\omega_c(t) + \Delta\omega_l(t))\, t\right) \quad (1)$$

The output signal of the SILO is frequency-modulated (FM) by the Doppler phase shifts of the echo signals as presented in (1), where A_{SILO} and ω_{SILO} are the intrinsic amplitude and frequency of the SILO, respectively.

$$\Delta\omega_c(t) = \omega_{LR,c} \sin\left(\frac{2\omega_{SILO}}{c}\left(D_c + d_r(t)\right)\right) \quad (2)$$

$$\Delta\omega_l(t) = \omega_{LR,l} \sin\left(\frac{2\omega_{SILO}}{c}\left(D_c + (z + d_h(t))\sqrt{\varepsilon_{r,m}}\right)\right) \quad (3)$$

Equations (2) and (3) provide a detailed perspective on frequency modulation of the SILO's locking range functions [16]. In these equations, ω_{LRc} and $\omega_{LR,l}$ are proportional to the magnitude of the echo signals from the chest and the flexible transmitarray lens, respectively, D_c is a distance, z is the focal length, c denotes the speed of light, $\varepsilon_{r,m}$ is a dielectric constant of the chest muscle, $d_r(t)$ and $d_h(t)$ are the relative movement between the transmitter and the chest-affixed flexible lens and also specify the instantaneous displacement due to respiration and heartbeat, respectively.

$$\omega_{\text{LR}} = \frac{\omega_{\text{SILO}} A_{\text{ec}}}{2Q A_{\text{SILO}}} \quad (4)$$

So, both ω_{LRc} and $\omega_{LR,l}$, are grounded from Adler's equation [32] defined by ω_{LR} in (4). Note that Q represents the quality factor of the (SILO), while A_{ec} represents the amplitude of the echo signal. SILO circuits employ a clapp structure, wherein the injection port is intricately linked to the transistor gate. This setup has a transmit power of approximately 2 dBm with a power consumption of 330 mW and 200 MHz bandwidth. The radar transmitted the SILO output signal via the antenna array to the subject and receives the echo signal that is injected into the SILO system. Subsequently, the signal undergoes low-noise amplification using a low-noise amplifier (LNA) with a very narrow bandwidth. After amplification, the signal is directed to the delay line frequency demodulator [33]. We obtain the frequency modulation $\Delta\omega(t)$ by computing the arctangent of the in-phase ($I(t)$) and the quadrature component ($Q(t)$) that

are extracted from the demodulator [34], as described by

$$\Delta\omega(t) \approx \frac{1}{\tau_d}\left(\tan^{-1}\frac{Q(t)}{I(t)}\right) - \omega_{\text{SILO}}. \quad (5)$$

The symbol τ_d signifies the temporal delay introduced by the delay line present within the demodulator. When the electrical length of $d_h(t)$ at ω_{SILO} is insignificant, (3) can be approximated as

$$\frac{\omega_{\text{SLO}}d_h(t)\sqrt{\varepsilon_{r,m}}}{c} \approx \frac{\Delta\omega_l(t)}{2\omega_{LR,l}\sin\left(2\omega_{\text{SIIO}}\left(D_c + z\sqrt{\varepsilon_{r,m}}\right)/c\right)}$$
$$- \frac{\tan\left(2\omega_{\text{SLO}}\left(D_c + z\sqrt{\varepsilon_{r,m}}\right)/c\right)}{2}. \quad (6)$$

The heart movement, represented by $d_h(t)$, is calculated using (5) and (6). The resultant movement signal undergoes further processing to isolate the heartbeat signal. As depicted in Fig. 1, the radar system operates at 5.8 GHz and utilizes an antenna positioned at a distance $D_c = 1$ meter from the flexible transmitarray lens, which is worn on the chest with a focal point $(0, 0, z)$ and a coordinate point $(x, y, 0)$. The frequency demodulator detects the SILO's frequency modulation, which is digitally recorded by a data acquisition (DAQ) system. These captured data are analyzed by a computer to determine the beat-to-beat interval (BBI), providing detailed heartbeat information.

III. RADAR ANTENNA

The SIL Doppler radar antenna is specifically designed for a 3–8 GHz bandwidth, featuring a smaller beamwidth of less than $17°$. This design incorporates high gain, narrow beamwidth, sensitivity, and excellent efficiency to optimize the power of the radar system. By focusing the transmitted and received electromagnetic waves in a specific direction, it maximizes the system's capabilities. The array antenna is designed with a three-band structure, providing multiple operating frequencies. Its input impedance ranges from $150-337\ \Omega$, allowing flexibility and compatibility with various systems. The proposed configuration of the antenna array depicted in Fig. 2, has overall dimensions of 52×44 mm. It utilizes a dielectric substrate with a 1.6 mm thickness, a relative permittivity (ε_r) of 3.5, loss tangent ($\tan\delta$) of 0.02, and relative permeability of 1.

The offered antenna array consists mainly of two identical pairs of U-slots. One substrate contains four radiating elements in the upper layer, whereas another substrate comprises the ground and the feed line in the lower layer. An impedance SMA connector $50-\Omega$ is used at the termination of the antenna feed line to transmit the input RF signal (Fig. 1), minimizing signal reflections and improving power transfer efficiency. Incorporating multilayer designs into antenna arrays aims to enhance bandwidth and radiation patterns by leveraging differences in layer thicknesses and dielectric constants to achieve desired features [35]. The inclusion of an air gap in an antenna array design offers several advantages. First, it provides isolation between elements, reducing mutual coupling [36] and interference, thus improving the integrity of the signal and overall performance. Second, the air gap minimizes crosstalk, resulting in cleaner signals and reduced interference. Moreover, it provides the ability to
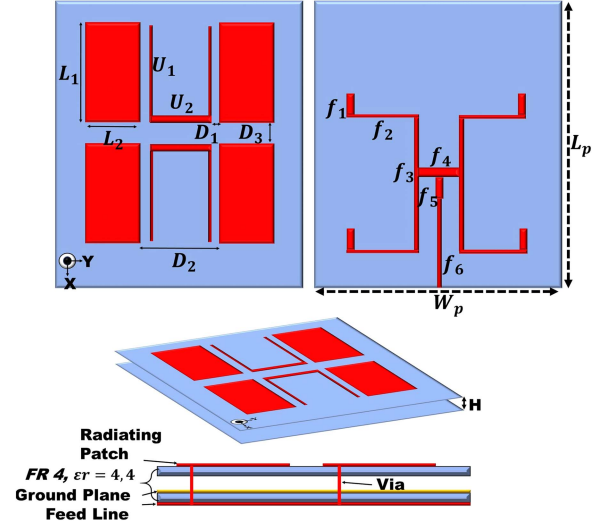

Fig. 2. Proposed architecture design of a multi-band radar array antenna.

TABLE I
ARCHITECTURE STRUCTURE OF THE SUGGESTED MULTIBAND RADAR ARRAY ANTENNA

Parameters	Size (mm)	Parameters	Size (mm)	Parameters	Size (mm)
Lp	52	D2	17.3	F3	0.77
Wp	44	D3	7.2	F4	1.3
H	4.2	U1	1	F5	1.3
D1	2.8	U2	1.25	F6	0.77
L1	17	F1	1	H	4.2
L2	9.5	F2	0.5	Via	0.8

accurately regulate the radiation pattern of each element, and the overall matrix contributes to superior overall performance [37].

Fig. 2 illustrates the proposed antenna array architecture, consisting of square patches with 2×2 radiating elements and two U-slots in the upper layer. Vias with a diameter of 0.8 mm are utilized to establish the connection between the feed line in the bottom layer and the four radiating elements. The feeding network consists of a one-to-four power divider and a transmission line that is soldered to the $50-\Omega$ coaxial SMA connector. Table I shows the parameters of the proposed construction, including specifics on its size and geometric features.

A novel three-band antenna array with U-shape patch has been proposed with a simple configuration. It integrates 3.81, 5.8, and 8.8 GHz into a multi-layer substrate, performing high gains of 12.2, 13.8, and 11.1 dBi at those frequencies. The U-shaped metasurface patch design helps reduce interference from unwanted directions or signals [38]. By shaping the radiation pattern, the antenna can focus its energy toward the desired direction while attenuating signals from other directions, enhancing signal quality, and reducing interference. In general, the U-shaped patch in the antenna array design offers improved return loss, reduced interference, mutual coupling [39] and increased gain [40].

Fig. 3(a) illustrates the comparison between the proposed structure for antenna arrays without U-slot, using one U-slot, and two U-slots. It is observed that the implementation of the
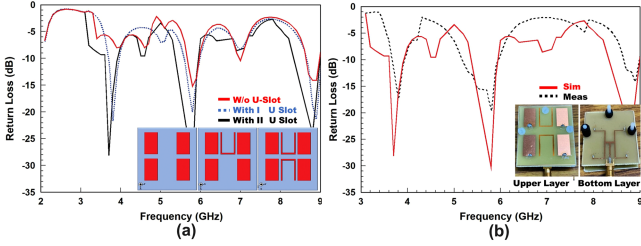
Fig. 3. Return loss $S11$ comparison of (a) with U-Slot and without using U-Slot. (b) Performance comparison between simulated-measured U-slot.
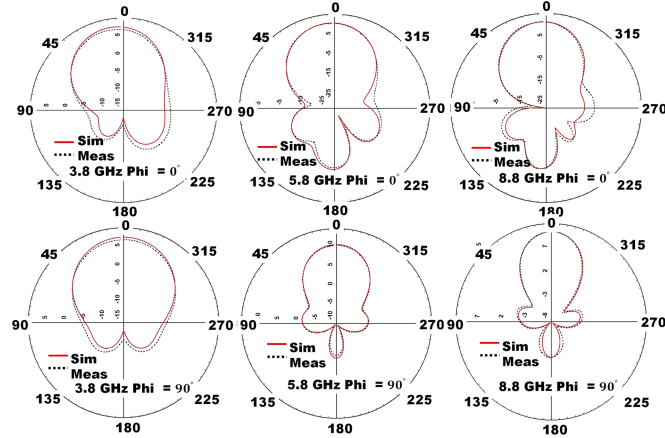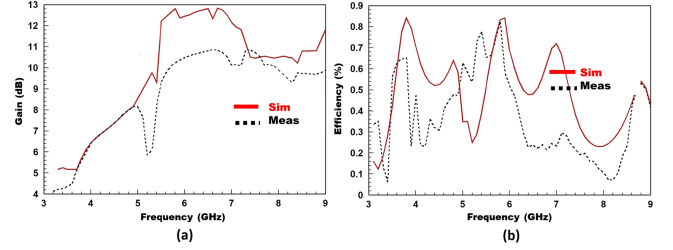

Fig. 5. Three discrete frequency bands (a) gain and (b) efficiency were evaluated and compared through both empirical measurement and sophisticated computer simulations of U-shaped patch.

Fig. 4. U-shaped radiation pattern measured and simulated for $\phi = 0°$ and $\phi = 90°$.

two U slots in the antenna array improves return loss and bandwidth. This corresponds to a bandwidth enhancement of 50%, indicating the achievement of enhanced gain and bandwidth in the desired frequency band. Fig. 3(b) shows the return loss of the simulations and measurements with the visual expression of the physical implementation of the U-shape design. The return loss denoted as (S_{11}) of 27.151dB, 32.243dB and 24.017 demonstrates favorable values at frequencies of 3.81,5.8 and 8.8 GHz. Additionally, the antenna has a bandwidth of 113, 403.7, and 500.88 MHz in a frequency range of 3.65–3.85, 5.5–5.9 and 8.4–8.8 GHz. Significantly, the measured reflection coefficient closely corresponds to the simulated results, providing further validation for the accuracy of the calculations. To enhance isolation performance, a cutting-edge dual U-slot patch metamaterial is seamlessly integrated at the focal point of the antenna elements. This arrangement significantly improves isolation, exceeding -20 dB in the three operating bands, mitigating interference. The decoupling element can be seen as a type of electromagnetic bandgap (EBG) structure [41], which occupies minimal space compared to previously reported designs [42].

The estimated radiation patterns at the specified design frequencies of 3.81, 5.8, and 8.8 GHz are shown in Fig. 4. Radiation patterns are presented in the $\phi = 0°$ and $\phi = 90°$ planes, with normalization applied for clarity. The radiation patterns of the proposed antenna exhibit symmetrical features, focusing on a specific and narrow direction. Across a range of frequencies,

the simulated and measured results display a notable level of agreement, signifying a strong consistency between the two sets of data. The proposed antenna exhibits a measured H-plane 3-dB beamwidth of $45°$, $39°$, and $42.5°$ at frequencies of 3.81, 5.8, and 8.8 GHz. With their expansive H-plane radiation patterns, this provides comprehensive coverage of the azimuth plane when multiple panels are utilized.

Figs. 5(a) and 5(b) illustrate the measured gain and efficiency of the antenna array with the U-shaped patch. According to the findings, the measured gain is 5.6 dB at 3.81 GHz, with an accompanying efficiency of 62%. Within the 5.8 GHz band, the measured gain exceeds 10.2 dB and the productivity reaches 73%. At 8.8 GHz, the quantified improvement is 9.33 dB, while the efficiency is 51%. These results clearly indicate that high gain is present across all three desired frequency bands, thereby ensuring excellent sensing directivity and sensitivity, which are vital for intended applications.

In conclusion, the U-shaped patches in the antenna design significantly enhance gain, providing a focused and directed radiation pattern ideal for precise and sensitive signal detection, crucial for healthcare radar systems. These characteristics ensure accurate monitoring of biological signals such as breathing or heartbeats, with minimal interference. Furthermore, the U-shaped patch design attributes make the antenna compatible with our suggested flexible transmitarray lens, offering directional transmission, flexibility, and improved bandwidth, essential for various wireless applications.

IV. WEARABLE FLEXIBLE TRANSMITARRAY LENS

A. Design of Unit Cell

In Fig. 6(a), the proposed layout of the transmitarray lens with W = 7 mm in a square area, which corresponds to 0.12 λ at 5.8 GHz. The lens comprises four metallic copper-layers for better control of the electromagnetic properties and enhanced performance compared to single-layer substrates [43]. Even layers have a cross pattern, and odd layers have a circular pattern with radius $0.9 - 4.7$ mm according to optimization technique. The substrate between the metal layers is made of polyimide (PI). The characteristics include a dielectric constant of $\varepsilon_r = 3.5$, a tangent loss of $\tan \delta = 0.0027$, and a layer thickness of $h_1 = 50.8$ μm. The total substrate thickness with stacked layer is 152.4 μm [44].
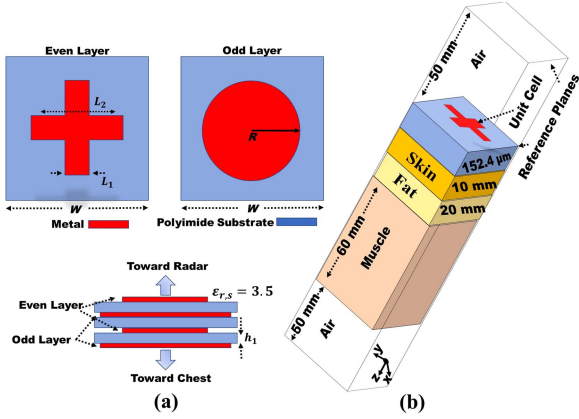
Fig. 6. (a) Unit cell architecture of the transmitarray lens ($L_1 = 1$ mm, $L_2 = 4$ mm, W = 7 mm, R = 3 mm). (b) Electromagnetic setup using HFSS floquet port.

TABLE II
TRANSMISSION COEFFICIENTS ACROSS UNIT CELL WITH DIVERSE DIMENSIONS

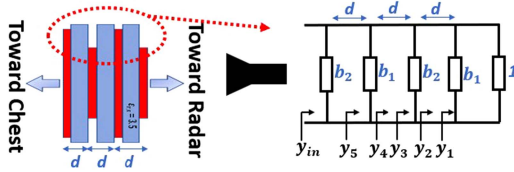| Size.		Transmission coeff.			
Odd Layer 1 (mm)	Odd Layer II (mm)	Mag I	Phase I (deg)	Mag II	Phase II (deg)
0.9	7.2	0.57	−3.48457	0.63	77.67
1.7	6.3	0.89	−4.42128	0.56	62.237
3.7	5.43	0.94	−15.7975	0.83	51.36
4.3	4.6	0.82	−26.221	0.57	30.44
4.7	2.1	0.63	−36.4581	0.44	10.12

Fig. 7. Simplified equivalent circuit model is employed for a four-layer copper flexible transmitarray, where the values are normalized.

The optimized design of the unit cells, achieved through simulation using ANSYS (HFSS) software, is outlined in Table II. The simulation considered a practical scenario with a 50-mm air gap and employed Floquet port excitation. To ensure the real-world applicability of the transmitarray, additional factors were taken into account. Specifically, the simulation incorporated a 60 mm thick muscle, 20 mm fat, and 10 mm thick skin layer, both characterized by dielectric constants of $\varepsilon_r = 47.715$, $\varepsilon_r = 4.9549$ and $\varepsilon_r = 34.0914$, respectively. Fig. 6(b) provides a visual representation of this setup. By considering these practical aspects in the simulation, the optimized design of the transmitarray lens improves the accuracy and reliability of the design, ensuring its feasibility and performance in real-world scenarios.

A simplified circuit representation of each cell, as illustrated in Fig. 7, can effectively model the behavior of the cell [45]. In this circuit, the metalized layers are represented by the shunt admittances on the transmission lines, with normalized values denoted as b_1 and b_2. Then, in a proportional four-layer arrangement, the unit-cell elements in layers 2 and 4 demonstrate equal admittances [46]. The circuit's termination is accomplished by using a normalized free-space characteristic admittance set to 1.
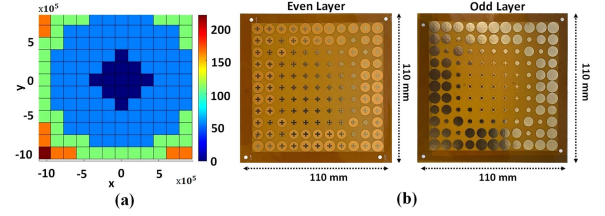

Fig. 8. (a) Metasurface optimization using Matlab. (b) Printed flexible transmitarray lens.

The sections of the transmission line with lengths of d represent the spacing between layers. This length takes into account the physical distance between the layers, along with an empirical correction for the substrate (in this case, the substrate thickness is 50.8 μm).

B. Flexible Transmitarray Lens Design

The phase distribution of the transmitarray lens, which underwent optimization using Matlab with reference to the values provided in Table II, is depicted in Fig. 8(a). Therefore, Fig. 8(b) presents an ultimate configuration of the transmitarray, showcasing a printed flexible polyimide design comprising 12×12 elements and a total square of 110×110 mm. The theoretical computation of $Z_{\max}$ is 90 mm or $2.12\lambda_0$, assuming a base angle of $\beta = 30°$ to achieve the desired energy distribution in a human heart valve.

Taking into account the equivalent circuit depicted in Fig. 8, we set y_{in} to 1 and rearrange the equation to express b_2 in terms of b_1.

$$b_2 = \frac{2\left(-b_1 + b_1 \tan(\beta d)^2 + b_1{}^2 \tan(\beta d)\right)}{b_1{}^2 \tan(\beta d)^2 + 1 + \tan(\beta d)^2 - 2b_1 \tan(\beta d)}. \tag{7}$$

To achieve a desired phase shift in a transmitarray, the process involves varying b_1 as an odd layer and calculating the corresponding b_2 as an even layer for different transmission phase values d. The transmission phase of the circuit is dictated by the transmission matrix, as indicated in Table II. Once b_1 is determined, the susceptibility value of b_2 is calculated using (7) to ensure proper match. Regardless of the shape of the elements, these two curves are influenced by the total layers, the physical partition [47], and the substrate thickness [48]. The same approach can be used for transmitarray cells with either two or four layers, as outlined in [49], although the matching conditions for b_2 will differ from (7).

Using an equivalent circuit represented in Fig. 7, the given equation derives the relationship between b_2 and b_1. Here, β represents the phase constant, which is determined by the operating frequency and the speed of light. b_1 and b_2 are normalized complex admittance values that characterize the behavior of the transmitarray cell. Their purpose is to accomplish the desired phase shift within the cell. The term $(\beta d)^2 + b_1^2$ in the equation represents a combination of the phase shift presented by the physical segregation between the layers (d) and the normalized admittance b_1. It affects the overall phase response of the transmitarray cell. By manipulating b_1 and calculating
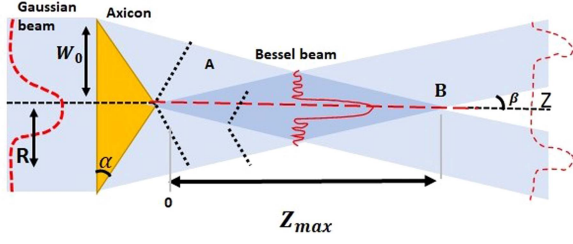
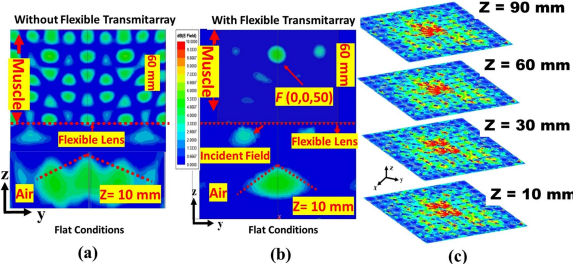Fig. 9. Illustration of a bessel beam generation using axicon.

Fig. 10. (a) Flat conditions: $Mag - E$ distribution in yz-plane without flexible transmitarray lens (b) Flat conditions: $Mag - E$ distribution in yz-plane with flexible transmitarray lens. (c) Flat conditions $Mag - E$ distribution of multiple planes in xy-plane along the z-axis.

the corresponding b_2 for different values of d, the transmission phase can be controlled and adjusted accordingly. It is necessary to note that the values of b_1 and b_2 are obtained by analysis and optimization, considering various factors such as the number of layers, partition in the physical layer, substrate thickness, and the desired phase shift in the transmitarray cell. These parameters are essential in designing efficient and effective transmitarray systems [50].

The proposed transmitarray lens needs to have a specific phase distribution φ to achieve a focusing effect, as described by the Bessel beam equation [46]. The equation is given as:

$$\varphi_1 = k_0 \sqrt{x^2 + y^2} \sin \beta \tag{8}$$

Here, k_0 represents the wave number, which is equal to 2π divided by the free-space wavelength λ_0. As illustrated in Fig. 9, the axicon base angle is denoted by β, and x and y Specify the horizontal and vertical distances from the focal point (x_0, y_0, z) and a position on the transmitarray lens $(x_0, y_0, 0)$. The focal length is equivalent to the non-diffracting distance z [51]. An important observation is that as the axicon base angle increases, there is a corresponding decrease in the maximum non-diffracting distance z, and vice versa, resulting in a closer focusing area to the lens. The optimal focusing distance is at $Z_{\max}/2$, where $Z_{\max}$ is the maximum distance of the focusing area. Increasing the radius R of the axicon's surface increases the maximum distance $Z_{\max}$, which can be computed by $Z_{\max} = R/\tan \beta$ [52].

C. Focusing Transmitarray in Different Planes

Fig. 10 illustrates the contrast in the penetration of the electric field into the chest with and without the use of a flexible transmitarray lens. In Fig. 10(a), it is evident that the electric

field distribution does not converge at the focal point (0,0,90) mm. On the contrary, Fig. 10(b) shows that the electric field penetrates successfully at the focal point (0,0,90) mm. Furthermore, Fig. 10(c) depicts the electric field distribution of a y-polarized incident wave when the transmitarray lens is illuminated at $Z = -10$ mm with significant non-scattered aspects. The simulated focusing distance ($Z_{\max}$) is 80 mm($2.02\lambda_0$), which is lower than the theoretically calculated value but still suitable for remote vital radar applications using a Gaussian beam within the Rayleigh distance. The simulated value β is the angle between the incident wave and the lens surface, which is $29.6°$ and is in close agreement with the theoretical prediction. When simulations are performed on different planes at distances of $Z = +10$ mm, $+30$ mm, $+60$ mm, $+90$ mm, the focusing efficiencies are $39.5\%, 49\%, 42\%, 27\%$.

In real implementations, the target orientation may vary, necessitating the derivation of the transmitarray beam deflection formula based on the generalized refraction law. This formula can be expressed as follows:

$$n_t \sin \theta_t - n_i \sin \theta_i = \frac{\lambda_0}{2\pi} \frac{d\Phi}{dl} \tag{9}$$

Here, the incident angle symbolized by θ_i, θ_t denotes the refraction angles, while the refractive index symbolized by n_i and n_t characterizes the refracted medium. Given the vertical incidence of the beam from the air, it traverses the transmitarray and subsequently refracts into the human body, leading to $\theta_i = 0$ and $n_i = n_t = 1$. This condition applies to the x and y directions, thus allowing us formulating the deflection equation as follows:

$$\varphi_2 = k_0 \sin (\theta_1) x + k_0 \sin (\theta_2) y \tag{10}$$

In this scenario, θ_1 and θ_2 represent the refraction angles in the x and y directions. Maintaining consistent energy transmission efficiency for Bessel beams within the focusing range is of great importance. The following equation is required for the efficiency computation [50]:

$$\eta = \frac{\oint \frac{1}{2} \text{Re} \left(\vec{E} \times \vec{H}^* \right) dS_1}{\oint \frac{1}{2} \text{Re} \left(\vec{E} \times \vec{H}^* \right) dS_2} \tag{11}$$

where $\eta =$ represents the average efficiency of transmission of power or energy, Re represents the real part of the quantity within parentheses. In this case, we have the cross product of two vectors $\vec{E}$ and $\overrightarrow{H^*}$ representing the electric field and the complex conjugate of the magnetic field, respectively [53], and d representing an infinitesimal area vector. The integral is taken over S_1 and S_2, which represent the cross-sectional regions of the focus region. Theoretically, the optimal focusing plane is found at $Z = Z_{m}ax/2$, where the greatest focusing diameter is reached with a radius of R. Thus, the focusing efficiency is determined by comparing the circular area of the focusing zone (S_1) with a diameter of R to the square area of the entire plane (S_2) with a side length of $2R$. Both surfaces are identical to the metasurface size [54]. By adhering to these design considerations, the proposed transmit array aligns with the expected theoretical outcomes and exhibits high efficiency at a distance of $Z = Z_{\max}/2$. Understanding the efficiency of the
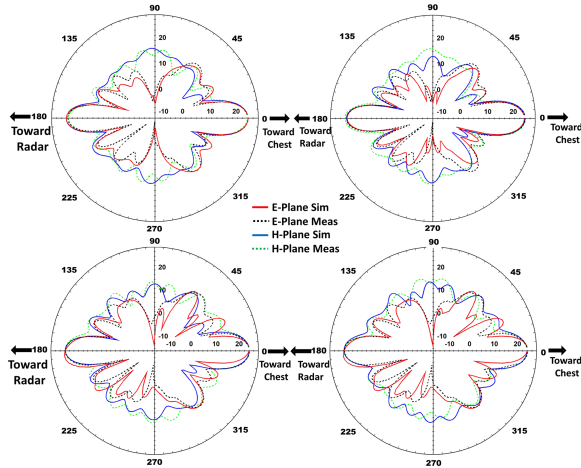
Fig. 11. Measured radiation patterns of the flexible transmitarray at $10°, 20°, 30°40°$ bending conditions in anechoic chamber.
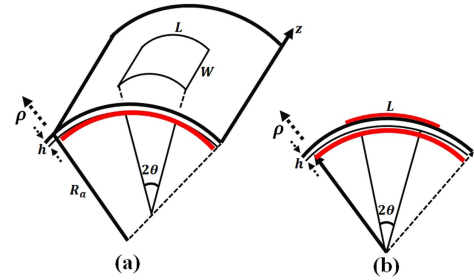

Fig. 12. (a) Portrayal of the transmitarray is contoured along the E-plane on a cylindrical surface, delineated by means of a geometric model, and (b) a principal perspective, presenting a graphical exposition of its tangible arrangement and configuration.

energy distribution in different planes facilitates accurate implementation and ensures proper functionality, even if the flexible transmit array experiences floating, bending, or unsteadiness at the desired distance.

D. Focusing Flexible Transmitarray in Bending Conditions

Moreover, it is crucial to note that within the focusing range, energy remains confined to the specific plane of that size, maintaining the desired characteristics. The design also accounts for bending conditions, and it has been observed that the unit cell experiences minimal stretching, while the substrate undergoes negligible contraction. Furthermore, the dielectric effects of the material remain consistent [55].

Fig. 11 shows the acquired radiation beam orientations, and the measured radiation patterns exhibit remarkable agreement with the simulated results for both the E- and H-plane radiation patterns at 5.8 GHz, even when subjected to diverse bending conditions. The transmitarray exhibits a maximum gain of 26.63 dB, and the 3-dB gain bandwidth spans 16.9% of the operating frequency. The antenna efficiency, taking into account the gain calculated by the aperture cross-section size, is determined to be 85.3%. The radiation patterns exhibit stability across the 5.8 GHz band. In terms of polarization performance, the measured cross-polarization level at 5.8 GHz is observed to be -29.8 dB, indicating a good level of cross-polarization suppression. The maximum sidelobe level is measured to be -13.4 dB.

However, the measured aperture efficiency is negligibly descending compared to the simulated value, with respective values of which are 65% and 78.9%. This discrepancy in aperture efficiencies could be attributed to various factors, including fabrication tolerances or measurement uncertainties. Despite the minor variations, it still demonstrates a reasonable level of efficiency in capturing and utilizing the available electromagnetic energy. The efficiency of the aperture η can be determined using the equation [56]:

$$\eta = \frac{G}{D_0}, \quad D_0 = \frac{4\pi A_e}{\lambda_0^2} \tag{12}$$

In this context, G stands for the approximated gain, D_0 signifies the maximum directivity, λ_0 represents the wavelength in free space, while A_e denotes the physical extent of the aperture. The proposed stacked-layer flexible transmitarray lens has a very good efficiency without the need for holes. The exceptional efficiency can be chiefly attributed to meticulous management of spillover and taper losses, registering at 0.52 dB and 0.41 dB, respectively [57], as well as transmission loss around 1.25 dB.

The illustration of the structured curved transmitarray as a cylindrical-rectangular cavity is presented visually in Fig. 12(a). The z-direction is confirmed to be the axis of the cylindrical surface where the unit cell is united. L is the transmitarray length $L = 110$ mm $\lambda/2$, W stands for the transmitarray width $W = 1.524\,\mu$m, substrate thickness is denoted by h, the cylindrical surface radius is Ra, and the estimated bending angle: $2\theta = L/(Ra + h)$. To represent different bending configurations, the bending angle 2θ and the inner bending radius a are adjusted accordingly. The eigenvalue, k, represents the wave number that propagates in the medium, $k = 2\pi/\lambda$. In the cavity architecture, where different bending angles are considered boundary conditions [58], the variation in the eigenvalue k signifies a change in the propagation wavelength λ within the medium [59]. The phase velocity remains constant when electromagnetic waves propagate at an identical frequency. $\nu = \lambda f = 1/\sqrt{\mu\varepsilon}$ [60]. The cavity structure obeys the Helmholtz equation, with the magnetic vector potential $\overrightarrow{A}$ and the electric vector potential $\overrightarrow{F}$ and the equation to be fulfilled within the cavity. The resonant frequencies differ for various modes, such as TEmli or TMmli, and can be determined using the following formula [61]:

$$f_{r,\mathrm{mli}} = \frac{1}{2\pi\sqrt{\epsilon\mu}}\sqrt{k_{mi}^2 + \left(\frac{l\pi}{2b}\right)^2} \tag{13}$$

The values of k_{mi} are found by solving (16) and (17) for the TEz modes (bending in the E-plane) and the TMz modes (bending in the H-plane) [59]:

$$J_v'(k_{mi}a)\,Y_v'(k_{mi}(a+h)) - J_v'(k_{mi}(a+h))\,Y_v'(k_{mi}a) = 0 \tag{14}$$
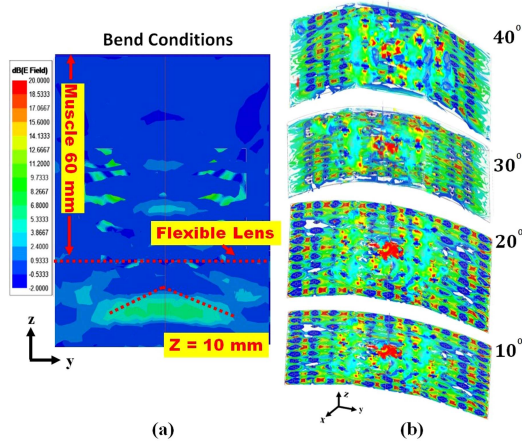
Fig. 13. Geometric model on the cylindrical surface of a transmitarray curved along the E-plane. (a) Bending Conditions $Mag - E$ distribution in the yz plane with Z = 10 mm. (b) Bending conditions: Mag-E distributions along the z-axis.

$$J_v\left(k_{mi}a\right)Y_v\left(k_{mi}(a+h)\right) - J_v\left(k_{mi}(a+h)\right)Y_v\left(k_{mi}a\right) = 0 \tag{15}$$

The Bessel functions J_v and Y_v correspond to the first and second categories. The parameter v indicates the bessel function order, which is defined as $v = m\pi/2\theta$. The prime sign in (14) and (15) represents the derivative of the statement of Bessel functions [55].

In the extreme case of a flat substrate, where there is no bending or curvature, the bending angle has a value of $2\theta = 0°$, and the bending radius approaches infinity ($a \to \infty$). In this case, the TE$_{101}$ eigenfrequency returns to the resonant frequency of the flat configuration, which can be defined as:

$$k_{mi} = \frac{m\pi}{2\theta a}, \quad f_{r,\text{mli}} = \frac{1}{2\pi\sqrt{\epsilon\mu}}\sqrt{\left(\frac{m\pi}{2\theta a}\right)^2} \tag{16}$$

Equation (14) is satisfied as the order of the Bessel function, denoted as v, tends to a significantly large number. Furthermore, it can be demonstrated that the TM$_{011}$ eigenfrequency also returns to the resonant frequency of the flat configuration, This satisfies (14) when $v = 0$, which given by:

$$k_{mi} = 0, \quad f_{r,\text{mli}} = \frac{1}{2\pi\sqrt{\epsilon\mu}}\sqrt{\left(\frac{l\pi}{2b}\right)^2} \tag{17}$$

Figs. 13(a) and 13(b) present a simplified model of the flexible structure under various bending angles. The simulation results support these findings by indicating that the resonance frequency of the transmitarray remains largely unaffected by bending in the E- and H-plane. The reason for this is that it has a minimal impact on the existing path of the fundamental resonance. Furthermore, by examining (13) for the fundamental mode TM$_{011}(m = 0, l = 1, i = 1)$, it can be observed that the order of the Bessel function, $v = m\pi/2\theta$, is equal to zero for various bending angles 2θ. To derive the electric field for varying bending angles along the E plane, the boundary conditions are meticulously satisfied [63] such as $10°$, $20°$, $30°$ and $40°$. The focus efficiency is acquired considering the gain determined by

TABLE III
SPESIFIC ABSORPTION RATE VALUE OF THE 5.8 GHZ TRANSMITARRAY

Human Tissue	Skin	Fat	Muscle
Relative Permittivity	34.0914	4.9549	47.715
Conductivity (S/m)	3.613	0.29113	4.3615
Mass Density (Kg/M^3)	1091	923	1050

the cross-sectional dimension of the aperture, which is 53.3%. The energy transmission of the non-diffracting Bessel beam should remain constant within the focusing range, both under flat and bent conditions [64].

In our study, we discuss the Specific Absorption Rate (SAR) [65], a crucial metric representing the rate at which the human body absorbs energy when exposed to an electromagnetic field of radio frequency (RF). Typically measured in watts per kilogram (W/kg), the relevance of SAR in this research lies in its critical role in ensuring the safety and effectiveness of the 5.8 GHz transmitarray lens for biomedical applications. Recognizing the importance of adhering to safety standards, we align our analysis with the regulatory guidelines established by authoritative bodies such as the FCC, which stipulate acceptable SAR limits to protect against adverse health effects. Our methodology for calculating SAR involves precise techniques and equipment that ensure accurate and reliable measurements. This rigorous approach allows us to evaluate the implications of the SAR values obtained, particularly focusing on their safety and efficacy dimensions in biomedical contexts. By meticulously analyzing SAR in relation to human tissue characteristics such as relative permittivity, conductivity, and mass density, the study not only adheres to the required safety norms but also advances the understanding of SAR's impact in the field of biomedical engineering. we investigated a streamlined three-layer flexible transmitarray lens constructed from polyimide with Ansys HFSS. This setup featured the flexible transmitarray lens placed on the human chest. The calculated SAR values obtained from this analysis are presented in Table III.

The SAR values outlined in Table III confirm that the system adheres to the safety guidelines established by both the Federal Communications Commission (FCC) and the International Commission on Non-Ionizing Radiation Protection (ICNIRP). This underscores that the use of a flexible transmitarray lens structure in SIL radar applications facilitates the attainment of minimal SAR values, for which no detrimental consequences have been identified.

Fig. 14(a) depicts the experimental setup used to analyze the received power in the focal plane of a transmitarray lens, attached to a 90 mm piece of pork meat, which simulates the dielectric properties of human muscle. Figs. 14(b) and 14(c) illustrate the comparison between simulated and actual measurements of the normalized received power distribution in the same plane, showing a notable match between them. In an optimally designed transmitarray aiming for beam focusing, one would anticipate a distinct bright region at the focal coordinates x_0, y_0, representing peak power reception. In contrast, zones farther from this focal coordinate should display reduced intensity with brighter color, signifying attenuated power levels, as the energy
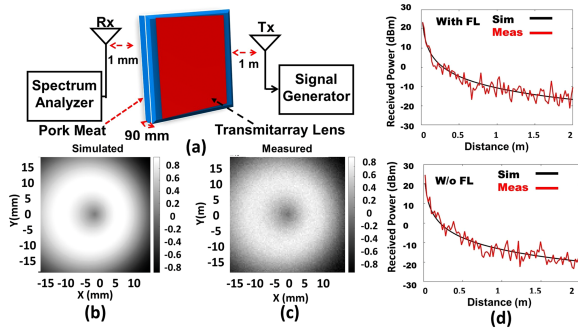
Fig. 14. Measuring the focusing effect of the transmitarray lens. (a) Measurement setup. (b) Simulated received power distribution on the focal plane. (c) Measured received power distribution on the focal plane (d) Simulated and experimental received powers with transmitarray at 5.8 GHz using meat pork.

TABLE IV
SIL RADAR COMPONENTS AND SPECIFICATIONS

Part	Implementations	Details
Antenna Array	PCB FR-4	Peak gain: 11 dBi Beamwidth: (H) 68° / (V) 66°
SILO	PCB FR-4	Power output : 5.6 dBm Spanning range: $5.7 - 6.1 GHz$
Frequency Demodulator	Coaxial Components	Gain conversion: 7 dB Delay: 22 ns

	Resting	Hand grip	Recovering
1	1 Min	2 Min	2 Min
	Resting	Cold stimulus 10'	Recovering
2	1 Min	2 Min	2 Min

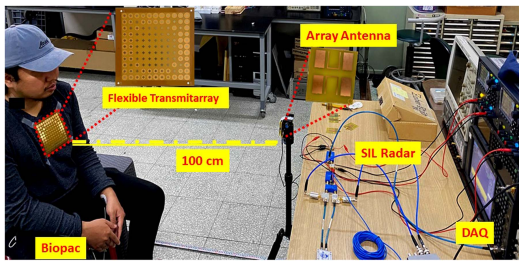Fig. 16. Illustration method for hand grip and ice cold pressure test challenge.

Fig. 15. Arrangement for vital signs detection of an individual in a seated position.

is being directed and concentrated toward the specified focal point. The recorded contour area of -4 dB is verified to be smaller than 15 mm × 15 mm, which confirms the sufficient focusing ability of the transmitarray lens. Although the received power level is subject to alteration due to the proximity of the pork meat to the receiving antenna, the shift related to the focal point remains approximately consistent. However, in Fig. 14(d) we investigate the received power levels at various distances between the transmitting and receiving antennas using pork meat as the medium. The transmitted power was set to 19 dBm, and the transmission was carried out at a frequency of 5.8 GHz using an antenna array with a gain of 13.8 dBi. With the adaptable flexible transmitarray lens attached, the received power was measured at -15 dBm. Without the transmitarray, the received power was lower, at -25 dBm. These results demonstrate the effectiveness of the transmitarray lens in enhancing the signal strength through a medium with a high dielectric constant. During the experimental measurements, the distances were systematically modified, and the resulting received power was carefully documented. Both experimental and theoretical results showed significant congruence, despite the presence of minor discrepancies attributed to various factors. These factors include environmental conditions, fabrication inconsistencies, SMA losses, RF cable losses, and other associated losses.

V. VITAL SIGN MONITORING SETUP AND RESULTS

Fig. 15 shows the arrangement used to monitor vital signs of a subject while sitting. The subject wears a flexible transmit array lens and an ECG is placed on their wrists and ankle according to the Einthoven triangle with an emphasis on lead I [63]. The 5.8-GHz SIL radar system serves as a key component in this configuration, emitting and detecting beams over 100 cm. The radar operates with a transmit power of 2 dBm and consumes 330 mW of power. The SIL radar system comprises an array antenna, a frequency demodulator, and a self-injection locked oscillator (SILO), all of which contribute to efficient signal acquisition. The transmit array lens is meticulously fastened to the individual's garment in proximity to the aorta, facilitating the effective aggregation and analysis of data. It functions to capture and bounce back a radar beam from a 5.8 GHz Doppler radar positioned 1 m away. Table IV presents details regarding the SIL radar components and specifications.

Two separate experiments, namely the hand-grip test challenge and the ice-cold test pressure challenge, were meticulously performed to accumulate physiological signals, as illustrated in Fig. 16. Throughout these experiments, participants were guided to maintain a relaxed posture and breathe naturally, all while in the vicinity of the SIL Radar and adorned with a flexible lens. The hand grip test required participants to exert pressure with their hands, while the ice-cold test elicited physiological responses by exposing them to cold stimuli. Despite substantial movements from participants, the use of the flexible transmit array lens effectively mitigated the impact of these movements, ensuring a steady focus of the radar beam. Due to variations in the structure of the human body and the lightweight, thin, and flexible nature of the suggested transmitarray lens, it could bend between 5° and 15° without compromising the performance of the antenna or the precision of vital sign detection. A total of four male subjects participated in these experiments (age 31.3 ± 22.4 years, height 165.9 ± 8.8 cm).

Fig. 17 emphasizes the improved accuracy in detecting vital sign information using the flexible lens. This advanced lens allows precise targeting of beam signals onto the heart valve, resulting in clearer and more detailed vital sign measurements. When utilizing the flexible lens, the specific spectrum frequencies recorded for breathing stand at 0.3 Hz, while those recorded for the heartbeat is 1.51 Hz. In contrast, without the use of this lens, the frequency for breathing reduces to 0.38 Hz and the heartbeat measurement drops to around 1.3 Hz. This
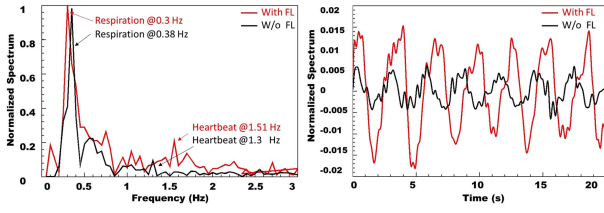
Fig. 17. Comparison of the vital sign waveforms and spectra obtained by using SIL radar with and without flexible Lens.
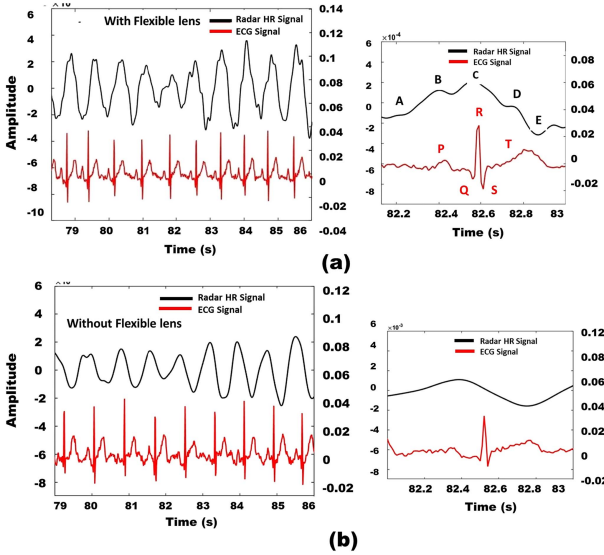

Fig. 18. Estimated normalized heartbeat wave from the self-injection locked (SIL) radar and comparing them with the peaks of the reference electrocardiogram (ECG) signal. (a) Extracted heartbeat waveform from SIL radar without flexible lens (b) extracted heartbeat waveform from SIL radar with flexible lens.

demonstrates the importance of the flexible lens in capturing accurate vital data. Fig. 18 provides a visual comparison of heartbeat waveforms obtained from the SIL radar, with and without the application of a flexible transmitarray lens. Fig. 18(a) presents the standardized heartbeat waveform obtained with an adaptable flexible transmitarray lens. However, Fig. 18(b) shows the standardized heartbeat waveform captured without an adaptable lens. The data clearly highlight the notable enhancement and stabilization of the heartbeat waveform when using the flexible transmit array and a comparison with the ECG as a reference. This improvement is attributed to the increased sensitivity and consistent stability provided by the flexible transmitarray throughout all the experiments carried out, confirming its significant impact on the reliability and accuracy of heartbeat waveform detection.

During the evaluation, our focus was predominantly on the deployment of an innovative adaptable transmitarray, which is meticulously designed for human chest attachment. Despite this primary focus, we extended the application of the flexible transmitarray to two distinct and challenging experimental scenarios: the handgrip test and the ice-cold test pressure. The successful implementation of these diverse tests underscored the transmitarray's robust performance and versatility,
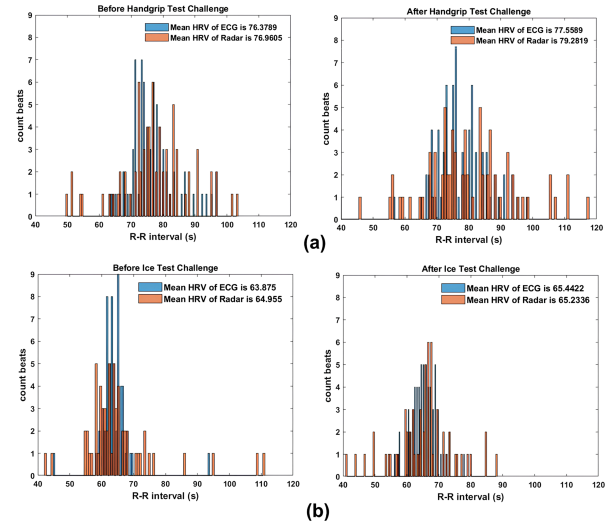

Fig. 19. Histogram (a) for hand-grip test challenge and (b) for ice cold test challenge, showing the heart rate in (beat per minute) comparison between the heartbeat signal from the SIL radar and the reference ECG signal before and after the test. The corresponding mean HR values are displayed in the legend.

confirming its capability to enhance and stabilize heartbeat waveform measurements across a range of conditions. In the course of these experiments, factors such as moving averages and body movements induced by the tests were present, potentially affecting the results. However, the flexible transmitarray proved instrumental in mitigating the impact of body movements, ensuring the reliability of the captured heartbeat waveform data. This effectiveness is largely attributed to the unique properties of the proposed transmitarray. It is exceptionally thin, lightweight, and flexible, perfectly conforming to the structure of the human chest when worn. These characteristics not only ensure comfort and convenience for the wearer, but also contribute substantially to the accurate and reliable monitoring of heartbeat waveforms, even in the face of external disturbances and movements.

The effectiveness of our flexible transmitarray, employed in conjunction with SIL radar, was rigorously validated by contrasting its performance with the established ECG measurements. Fig. 19 elucidates this comparison, presenting a detailed and methodical analysis of heart rate (HR) in beats per minute (bpm) during two different experimental scenarios: handgrip test challenge and ice-cold test pressure. In the histogram shown in Fig. 19(a), a comparative analysis of HR during the hand grip test challenge is depicted. HR values sourced from both the SIL radar (equipped with flexible transmitarray) and a reference ECG signal over a one-minute span were analyzed. Before the exercise, the radar recorded an average HR value of approximately 76.9605 bpm, closely aligned with the reference ECG average value of 76.3789 bpm. Post-exercise measurements exhibited an increase in HR for both methods, with the radar reporting an average of 79.2819 bpm and the reference ECG indicating an average of 77.5589 bpm. These data underscore a general elevation after exercise in average HR values. Proceeding further, Fig. 19(b) graphically presents the HR comparison between the SIL radar heartbeat signal and the reference ECG signal during
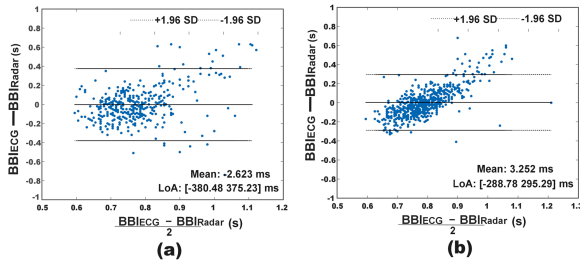
Fig. 20. Performance comparison beat-to-beat peak interval HR values between Radar and ECG using Bland-Altman plot: (a) for hand-grip test challenge, and (b) for ice cold test challenge.

the ice-cold test challenge. The legend meticulously details the corresponding mean HR values. Similarly to the observations made in the challenge of the handgrip test, a comparable trend was discerned, albeit with a different group of subjects.

To assess the agreement between Radar and ECG measurements, Bland-Altman plots were employed in the experiment. Fig. 20 presents the Bland-Altman plots for the same beat-beat interval values, which closely reflect the instantaneous heart rate. Figs. 20(a) and 20(b) are the hand grip test challenge and the ice-cold test challenge, respectively. The Bland-Altman analysis evaluates the differences in BBI values obtained from two distinct measurement techniques relative to their respective mean values. This statistical approach enables the assessment of agreement or discrepancy between the two methods, revealing potential variations in the measurement outcomes. The solid black line in this context represents the average difference between the methods, whereas the dashed black lines delineate the lower and upper limits of agreement (LoA). The limits of agreement (LoA) are estimated by adding and subtracting 1.96 times the standard deviation of the differences from the mean difference. Essentially, the LoA serves as a measure to establish the range within which most of the discrepancies between the two measurement methods are expected to lie. During analysis, a small fixed bias of -2.623 ms was observed in the hand grip test, while a bias of 3.252 ms was observed in the ice-cold test. The calculated LoAs were determined to be -380.48 ms and 375.23 ms for the hand-grip test, and -288.78 ms and 295.29 ms for the ice-cold test.

In this research, by precisely targeting the human heart rate, we are able to extract detailed information from the power spectrum density (PSD). It is typically challenging to discern the PSD, especially when the echo pulse signal waveform is disrupted by noise and the signal is not directly aimed at the human heart. Figs. 21(a) and 21(b) present an example of the power spectrum density (PSD) of HRV measured from both the SIL radar and the reference ECG. In Fig. 21(a), before the challenge of the hand grip test, the PSD HF range was relatively high in both the radar and ECG signals. Following completion of the exercise, there was a slight increase in PSD of HF PSD. Furthermore, the LF range exhibited a notable increase after hand grip challenge, indicating a change in the spectral characteristics associated with autonomic nervous system activity. Fig. 21(b) depicts the PSD from the ice pressure test challenge. The HF

value increased substantially, as well as the LF range increased. This analysis of power spectra provides valuable insight into the dynamic changes in HRV associated with different physiological conditions and interventions. It helps to elucidate the underlying mechanisms and responses of the cardiovascular system, contributing to a deeper understanding of human physiology and potential applications in health monitoring and assessment.

The power spectrum densities acquired from time series data of heartbeat intervals are examined in the frequency domain of heart rate variability (HRV) [66]. This analysis provides valuable information on the distribution of power across different frequency components within the HRV signal and helps identify specific frequency bands associated with physiological mechanisms and autonomic nervous system activity. To perform a spectral analysis of HRV, several steps were followed. Firstly, the beat-by-beat series, representing the time duration between successive heartbeats, were uniformly interpolated at a rate of 5 Hz [67]. This ensured consistent and evenly spaced data points, enabling accurate spectral analysis. The power spectra were then estimated using the Welch periodogram method, which involves dividing the data into overlapping segments and applying a Fourier transform to each segment. A 90% overlap was used to ensure sufficient data overlap for reliable spectral estimation.

To minimize any linear trends in the data, linear detrending was performed using Hann windows of 300 seconds in length. To enhance the spectral resolution and reduce noise, a broadband smoothing technique was applied. This involved applying a moving average to the power spectra, with the order of the moving average increasing with the spectral frequency. This smoothing process improved the coherence and interpretability of the spectral content. The power spectra obtained were summed within specific frequency bands that are important for analyzing heart rate variability (HRV). These bands include the very low frequency (VLF) range from 0.003 to 0.04 Hz, the low frequency (LF) range from 0.04 to 0.15 Hz, and the high frequency (HF) range from 0.15 to 0.4 Hz [68].

Tables V and VI provide a comprehensive summary of HRV indices in the frequency domain [69], [70], also the results of the Bland-Altman plot, utilizing data from four subjects. The Bland-Altman plot is a valuable tool for detecting systematic errors, such as fixed or proportional biases [71], in the measurements. The tables also include the natural logarithm of the components of LF and HF, normalized to the square of total power (s^2), which aids in the analysis and interpretation of HRV in the frequency domain. The R wave in the ECG waveform represents ventricular depolarization, while the RR interval signifies the duration of a full cardiac cycle. Calculating the average change in duration between successive RR intervals allows us to determine the heart rate variability (HRV) [72]. Additionally, the tables present PHF and PLF, representing high-frequency and low-frequency bands in the power spectrum density of heart rate fluctuations, respectively. These frequency bands provide valuable information on the modulation of heart rate by various physiological mechanisms, such as respiratory and autonomic activity.
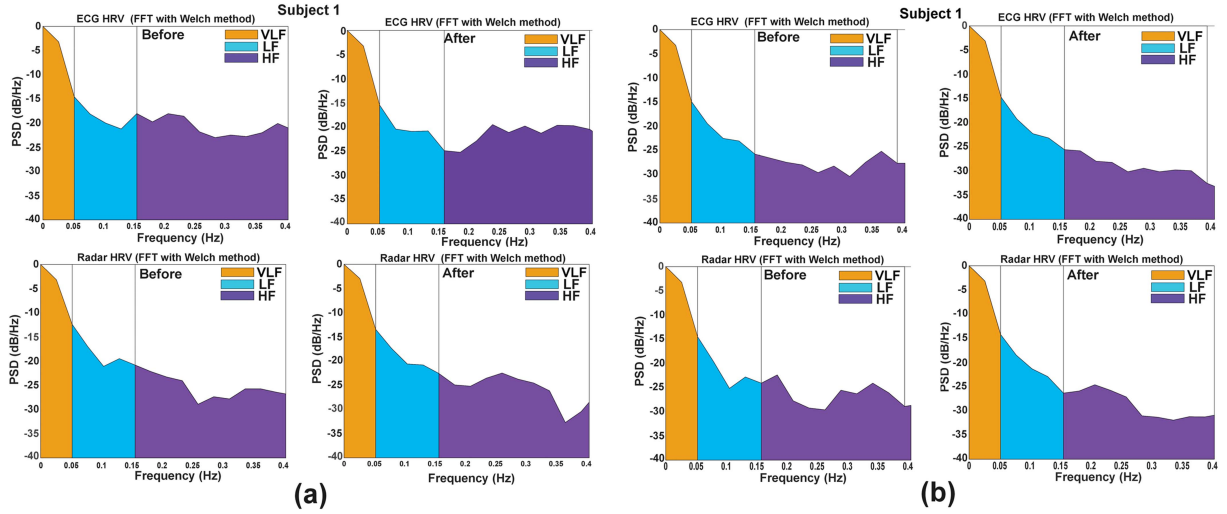
Fig. 21. Power spectrum distribution of HRV using SIL radar and the reference ECG signal. (a) Handgrip test challenge. (b) Ice test pressure challenge.

TABLE V
COMPARISON ESTIMATION OF CALCULATED HRVs FROM RADAR AND ECG AND HRV ESTIMATION RESULTS IN TERMS OF MEAN DIFF, MEAN DIFF BPM, AVG
HR RADAR AND ECG, AND AVG RR INTERVAL FOR 4 SUBJECTS DURING HANDGRIP TEST CHALLENGE

Subject	Hand-Grip Test Challenge	pLF (%)		pHF (%)		LFHFratio (s^2)		VLF (s^2)		LF (s^2)		HF (s^2)	
		Radar	ECG	Radar	ECG	Radar	ECG	Radar	ECG	Radar	ECG	Radar	ECG
1	Before	15.87	16.15	84.13	83.85	0.189	0.193	0.305	0.706	0.255	0.302	1.353	1.567
	After	29.77	29.78	70.23	70.22	0.424	0.424	0.164	0.517	0.750	0.680	1.768	1.604
2	Before	47.80	63.16	52.20	36.84	0.916	1.714	0.433	0.654	1.071	1.665	1.169	0.971
	After	43.03	53.20	56.97	46.81	0.755	1.137	0.380	0.442	1.100	1.407	1.456	1.238
3	Before	33.82	33.86	66.18	66.62	0.511	0.501	1.228	0.549	0.596	0.942	1.166	1.880
	After	21.11	25.07	78.89	74.93	0.268	0.335	0.130	0.408	0.540	0.362	2.019	1.081
4	Before	24.85	25.73	75.15	74.27	0.331	0.347	0.416	0.955	0.530	0.293	1.062	0.846
	After	33.92	33.06	66.08	66.94	0.513	0.494	0.556	0.301	0.712	0.481	1.386	0.975

TABLE VI
COMPARISON ESTIMATION OF CALCULATED HRVs FROM RADAR AND ECG AND HRV ESTIMATION RESULTS IN TERMS OF MEAN DIFF, MEAN DIFF BPM, AVG
HR RADAR AND ECG, AND AVG RR INTERVAL FOR FOUR SUBJECTS DURING COLD PRESSURE TEST CHALLENGE

Subject	Cold Pressure Test Challenge	pLF (%)		pHF (%)		LFHFratio (s^2)		VLF (s^2)		LF (s^2)		HF (s^2)	
		Radar	ECG	Radar	ECG	Radar	ECG	Radar	ECG	Radar	ECG	Radar	ECG
1	Before	48.68	47.28	51.32	52.73	0.948	0.897	0.481	0.791	1.157	1.219	1.220	1.360
	After	35.44	33.80	64.56	66.21	0.549	0.510	0.055	0.188	0.701	0.783	1.278	1.534
2	Before	36.80	35.02	63.20	64.98	0.582	0.539	0.124	1.292	0.99	0.79	1.70	1.46
	After	44.22	45.60	55.78	54.40	0.793	0.838	0.146	0.850	0.892	1.186	1.125	1.416
3	Before	46.10	40.42	53.90	59.58	0.855	0.678	0.097	0.372	1.160	1.265	1.356	1.865
	After	61.74	64.84	38.26	35.16	1.614	1.844	0.202	0.194	1.708	1.143	1.059	0.620
4	Before	43.73	42.65	56.27	57.35	0.777	0.744	0.545	0.135	0.925	0.732	1.191	0.985
	After	51.73	53.77	48.27	46.23	1.072	1.163	0.642	0.869	1.086	0.600	1.013	0.516

VI. CONCLUSION

This research paper introduces a new method that uses SIL radar technology with flexible transmit array lenses for the detection of vital signs. This methodology offers a significant advantage by enabling the radar wave beam to target a specific area of the thoracic region, thereby achieving a more precise detection of cardiac anomalies. The precision targeting afforded by this technique holds promise for integration into wearable technology, potentially leading to the development of smart clothing capable of continuous monitoring of heart health. This targeted approach allows for accurate measurement of vital signs while minimizing the impact of random body movements during experiments such as handgrip test and ice-cold test pressure resulting in improved system performance. This increased sensitivity enables for more accurate detection of the characteristics of the beat-by-beat interval (BBI) and heart rate variability (HRV), crucial indicators of cardiac activity. These advances contribute to the general precision and reliability of the radar system in capturing and analyzing various physiological parameters related

to heart activity. In conclusion, the proposed technique offers a valuable approach for remote sensor systems in pulse detection, demonstrating a moderate correlation between the detected heart rate and the reference values. This low-cost, lightweight, flexible and thin transmitarray lens has a potential impact that extends to various healthcare and monitoring applications, where real-time and noncontact vital sign detection plays a crucial role.

REFERENCES

[1] P. Wang, Y. Kim, L. H. Ling, and C. B. Soh, "First heart sound detection for phonocardiogram segmentation," in *Proc. IEEE Eng. Med. Biol. 27th Annu. Conf.*, 2005, pp. 5519–5522, doi: 10.1109/IEMBS.2005.1615733.

[2] J. Allen, "Photoplethysmography and its application in clinical physiological measurement," *Physiol. Meas.*, vol. 28, no. 3, 2007, Art. no. R1.

[3] V. K. Tallury and N.P. DePasquale, "Ultrasound cardiography in the diagnosis of left atrial thrombus," *Chest*, vol. 59, no. 5, pp. 501–503, 1971.

[4] U. Satija, B. Ramkumar, and M. S. Manikandan, "Automated ECG noise detection and classification system for unsupervised healthcare monitoring," *IEEE J. Biomed. Health Informat.*, vol. 22, no. 3, pp. 722–732, May 2018, doi: 10.1109/JBHI.2017.2686436.

[5] C. Yancy and W.T. Abraham, "Noninvasive hemodynamic monitoring in heart failure: Utilization of impedance cardiography," *Congestive Heart Failure*, vol. 9, no. 5, pp. 241–250, 2003.

[6] J.-C. Chiao et al., "Applications of microwaves in medicine," *IEEE J. Microw.*, vol. 3, no. 1, pp. 134–169, Jan. 2023, doi: 10.1109/JMW.2022.3223301.

[7] T. -S. Horng, "Self-injection-locked radar: An advance in continuous-wave technology for emerging radar systems," in *Proc. Asia-Pacific Microw. Conf.*, 2013, pp. 566–569, doi: 10.1109/APMC.2013.6694866.

[8] R. Bharadwaj and S. K. Koul, "Wearable UWB technology for daily physical activity tracking, detection, and classification," *IEEE Sensors J.*, vol. 22, no. 21, pp. 20684–20694, Nov. 2022, doi: 10.1109/JSEN.2022.3205116.

[9] M. P. Ebrahim, N. Tom, J. -M. Redoute, and M. R. Yuce, "A low-frequency portable continuous wave radar system for vital signs monitoring," *IEEE Sensors J.*, vol. 23, no. 8, pp. 8876–8886, Apr. 2023, doi: 10.1109/JSEN.2023.3251978.

[10] D. Buxi et al., "Systolic time interval estimation using continuous wave radar with on-body antennas," *IEEE J. Biomed. Health Informat.*, vol. 22, no. 1, pp. 129–139, Jan. 2018, doi: 10.1109/JBHI.2017.2731790.

[11] F.-K. Wang, T. -S. Horng, K. -C. Peng, J. -K. Jau, J.-Y. Li, and C.-C. Chen, "Single-antenna Doppler radars using self and mutual injection locking for vital sign detection with random body movement cancellation," *IEEE Trans. Microw. Theory Techn.*, vol. 59, no. 12, pp. 3577–3587, Dec. 2011, doi: 10.1109/TMTT.2011.2171712.

[12] P. H. Juan, H. C. Tsai, and F.-K. Wang, "Wearable vital sign sensing radar antenna with moving clutter immunity," in *Proc. IEEE Int. Symp. Radio- Freq. Integration Technol.*, Hiroshima, Japan, 2020, pp. 247–249, doi: 10.1109/RFIT49453.2020.9226235.

[13] F. -K. Wang, Y.-R. Chou, Y.-C. Chiu, M.-C. Tang, and T. -S. Horng, "Chest-worn health monitor based on a bistatic self-injection-locked radar," in *Proc. IEEE MTT-S Int. Microw. Symp.*, Phoenix, AZ, USA, 2015, pp. 1–4, doi: 10.1109/MWSYM.2015.7167083.

[14] R. E. Arif, M. C. Tang, W. C. Su, T. S. Horng, F.-K. Wang, and C.-H. Tseng, "Designing a metasurface-based tag antenna for wearable vital sign sensors," in *Proc. IEEE MTT-S Int. Microw. Symp.*, Boston, MA, USA, 2019, pp. 373–376, doi: 10.1109/MWSYM.2019.8700933.

[15] C.-H. Tseng and C. Z. Wu, "A novel microwave phased- and perturbation-injection-locked sensor with self-oscillating complementary split-ring resonator for finger and wrist pulse detection," *IEEE Trans. Microw. Theory Techn.*, vol. 68, no. 5, pp. 1933–1942, May 2020, doi: 10.1109/TMTT.2020.2966188.

[16] C.-H. Tseng, T. J. Tseng, and C. Z. Wu, "Cuffless blood pressure measurement using a microwave near-fieldself-injection-locked wrist pulse sensor," *IEEE Trans. Microw. Theory Techn.*, vol. 68, no. 11, pp. 4865–4874, Nov. 2020, doi: 10.1109/TMTT.2020.3011446.

[17] R. E. Arif, W. C. Su, and T. S. Horng, "Chest-worn heart rate variability monitor with a self-injection-locked oscillator tag," *IEEE Trans. Microw. Theory Techn.*, vol. 70, no. 5, pp. 2851–2860, May 2022, doi: 10.1109/TMTT.2022.3155185.

[18] F.-K. Wang et al., "Review of self-injection-locked radar systems for noncontact detection of vital signs," *IEEE J. Electromagn., RF, Microw. Med. Biol.*, vol. 4, no. 4, pp. 294–307, Dec. 2020, doi: 10.1109/JERM.2020.2994821.

[19] F. K. Wang et al., "A novel vital-sign sensor based on a self-injection-locked oscillator," *IEEE Trans. Microw. Theory Techn.*, vol. 58, no. 12, pp. 4112–4120, Dec. 2010, doi: 10.1109/TMTT.2010.2087349.

[20] A. Singh and V. M. Lubecke, "Respiratory monitoring and clutter rejection using a CW Doppler radar with passive RF tags," *IEEE Sensors J.*, vol. 12, no. 3, pp. 558–565, Mar. 2012, doi: 10.1109/JSEN.2011.2134083.

[21] A. Mishra and C. Li, "A low power 5.8-GHz ISM-Band intermodulation radar system for target motion discrimination," *IEEE Sensors J.*, vol. 19, no. 20, pp. 9206–9214, Oct. 2019, doi: 10.1109/JSEN.2019.2926189.

[22] W. McDonnell, A. Mishra, and C. Li, "Comprehensive vital sign detection using a wrist wearable nonlinear target and a 5.8-GHz ISM band intermodulation radar," in *Proc. IEEE Radio Wireless Symp.*, San Antonio, TX, USA, 2020, pp. 123–126, doi: 10.1109/RWS45077.2020.9049979.

[23] S. K. Behera, "Chipless RFID sensors for wearable applications: A review," *IEEE Sensors J.*, vol. 22, no. 2, pp. 1105–1120, Jan. 2022, doi: 10.1109/JSEN.2021.3126487.

[24] S. Vora, K. Dandekar, and T. Kurzweg, "Passive RFID tag based heart rate monitoring from an ECG signal," in *Proc. 37th Annu. Int. Conf. IEEE Eng. Med. Biol. Soc.*, 2015, pp. 4403–4406, doi: 10.1109/EMBC.2015.7319371.

[25] C. Wang, L. Xie, W. Wang, Y. Chen, Y. Bu, and S. Lu, "RF-ECG: Heart rate variability assessment based on cots RFID tag array," *Proc. ACM Interactive, Mobile, Wearable Ubiquitous Technol.*, vol. 2, no. 2, pp. 1–26, 2018.

[26] H. Lyu, Z. Wang, and A. Babakhani, "A UHF/UWB hybrid RFID tag with a 51-m energy-harvesting sensitivity for remote vital-sign monitoring," *IEEE Trans. Microw. Theory Techn.*, vol. 68, no. 11, pp. 4886–4895, Nov. 2020.

[27] K. Bayoumy et al., "Smart wearable devices in cardiovascular care: Where we are and how to move forward," *Nature Rev. Cardiol.*, vol. 18, no. 8, pp. 581–599, 2021.

[28] R. El Arif, W. C. Su, T. S. Horng, and C. -T. M. Wu, "Chest-worn transmitarray lens for monitoring heart rate variability with a remote self-injection-locked doppler radar," in *Proc. IEEE/MTT-S Int. Microw. Symp.*, San Diego, CA, USA, 2023, pp. 1188–1191, doi: 10.1109/IMS37964.2023.10188195.

[29] L. Blanc, A. Delchambre, and P. Lambert, "Flexible medical devices: Review of controllable stiffness solutions," *Actuators*, vol. 6, no. 3, 2017, Art. no. 23.

[30] Y. Khan, A.E. Ostfeld, C.M. Lochner, A. Pierre, and A.C. Arias, "Monitoring of vital signs with flexible and wearable medical devices," *Adv. Mater.*, vol. 28, no. 22, pp. 4373–4395, 2016.

[31] X. Wang, M. S. Tong, and G. -M. Yang, "Multifocus multinull near-field transmitting focused metasurface," *IEEE Trans. Antennas Propag.*, vol. 71, no. 4, pp. 3172–3182, Apr. 2023, doi: 10.1109/TAP.2023.3240538.

[32] R. Adler, "A study of locking phenomena in oscillators," *Proc. IRE*, vol. 34, no. 6, pp. 351–357, Jun. 1946, doi: 10.1109/JRPROC.1946.229930.

[33] F. K. Wang, C. H. Fang, T. S. Horng, K. C. Peng, J. Y. Li, and C. C. Chen, "Concurrent vital sign and position sensing of multiple individuals using self-injection-locked tags and injection-locked I/Q receivers with arctangent demodulation," *IEEE Trans. Microw. Theory Techn.*, vol. 61, no. 12, pp. 4689–4699, Dec. 2013.

[34] H. Gheidi and A. Banai, "An ultra-broadband direct demodulator for microwave FM receivers," *IEEE Trans. Microw. Theory Techn.*, vol. 59, no. 8, pp. 2131–2139, Aug. 2011, doi: 10.1109/TMTT.2011.2144993.

[35] M. Li, Y. Yang, F. Iacopi, J. Nulman, and S. Chappel-Ram, "3D-Printed low-profile single-substrate multi-metal layer antennas and array with bandwidth enhancement," *IEEE Access*, vol. 8, pp. 217370–217379, 2020, doi: 10.1109/ACCESS.2020.3041232.

[36] S. Farsi, H. Aliakbarian, D. Schreurs, B. Nauwelaers, and G. A. E. Vandenbosch, "Mutual coupling reduction between planar antennas by using a simple microstrip U-section," *IEEE Antennas Wireless Propag. Lett.*, vol. 11, pp. 1501–1503, 2012, doi: 10.1109/LAWP.2012.2232274.

[37] S. Ji, J. Hirokawa, and T. Tomura, "A wideband and high-gain all-metallic perpendicular-corporate-fed multi-layered parallel-plate slot array antenna," *IEEE Access*, vol. 10, pp. 38000–38011, 2022, doi: 10.1109/ACCESS.2022.3165121.

[38] A. Uluslu, "Chameleon swarm algorithm assisted optimization of U-slot patch antenna for quad-band applications," *IEEE Access*, vol. 10, pp. 74152–74163, 2022, doi: 10.1109/ACCESS.2022.3190378.

[39] M. Teng, S. Yu, N. Kou, Z. Ding, and Z. Zhang, "Mechanical beam steering array antenna with tunable height," *IEEE Antennas Wireless Propag. Lett.*, vol. 21, no. 11, pp. 2293–2297, Nov. 2022, doi: 10.1109/LAWP.2022.3181162.

[40] T. -Q. Fan, B. Jiang, R. Liu, J. Xiu, Y. Lin, and H. Xu, "A novel double U-slot microstrip patch antenna design for low-profile and broad bandwidth applications," *IEEE Trans. Antennas Propag.*, vol. 70, no. 4, pp. 2543–2549, Apr. 2022, doi: 10.1109/TAP.2021.3125382.

[41] S. Kim, D. K. Kim, Y. Kim, J. Choi, and K. -Y. Jung, "A 24 GHz ISM-Band Doppler radar antenna with high isolation characteristic for moving target sensing applications," *IEEE Antennas Wireless Propag. Lett.*, vol. 18, no. 7, pp. 1532–1536, Jul. 2019, doi: 10.1109/LAWP.2019.2922008.

[42] J. F. Gao and F. H. Lin, "Modeling and analysis of wideband multilayer metasurface antenna array using characteristic-mode analysis," *IEEE Trans. Antennas Propag.*, vol. 71, no. 3, pp. 2832–2836, Mar. 2023, doi: 10.1109/TAP.2023.3234201.

[43] S. Pandi, C. A. Balanis, and C. R. Birtcher, "Analysis of wideband multilayered sinusoidally modulated metasurface," *IEEE Antennas Wireless Propag. Lett.*, vol. 15, pp. 1491–1494, 2016, doi: 10.1109/LAWP.2015.2514241.

[44] K. Kamogawa, T. Tokumitsu, and M. Aikawa, "Multifrequency microstrip antennas using alumina-ceramic/polyimide multilayer dielectric substrate," *IEEE Trans. Microwave Theory Techn.*, vol. 44, no. 12, pp. 2431–2437, Dec. 1996, doi: 10.1109/22.554575.

[45] F. Costa, "A simple effective permittivity model for metasurfaces within multilayer stratified media," *IEEE Trans. Antennas Propag.*, vol. 69, no. 8, pp. 5148–5153, Aug. 2021, doi: 10.1109/TAP.2021.3060493.

[46] C.A. Balanis, *Advanced Engineering Electromagnetics*, Hoboken, NJ, USA: Wiley, 2012.

[47] X. Liu, M. Shu, X. Chen, and A. Zhang, "Four-dimensional characteristic matrix for electromagnetic coupling of multilayer sub-wavelength metasurface system," *IEEE Trans. Electromagn. Compat.*, vol. 62, no. 6, pp. 2765–2772, Dec. 2020, doi: 10.1109/TEMC.2020.2987826.

[48] H. Nematollahi, J. -J. Laurin, J. E. Page, and J. A. Encinar, "Design of broadband transmitarray unit cells with comparative study of different numbers of layers," *IEEE Trans. Antennas Propag.*, vol. 63, no. 4, pp. 1473–1481, Apr. 2015, doi: 10.1109/TAP.2015.2402285.

[49] Z. -W. Miao, Z. -C. Hao, D. -Q. Yu, C. -Y. Ding, and F. Wu, "A W-band high-gain bilayer transmit-array antenna employing huygens resonance," *IEEE Antennas Wireless Propag. Lett.*, vol. 22, no. 5, pp. 1184–1188, May 2023, doi: 10.1109/LAWP.2023.3235989.

[50] S. Li, Z. N. Chen, T. Li, F. H. Lin, and X. Yin, "Characterization of metasurface lens antenna for Sub-6 GHz dual-polarization full-dimension massive MIMO and multibeam systems," *IEEE Trans. Antennas Propag.*, vol. 68, no. 3, pp. 1366–1377, Mar. 2020, doi: 10.1109/TAP.2020.2968849.

[51] Z. Wang et al., "High-efficiency generation of bessel beams with transmissive metasurfaces," *Appl. Phys. Lett.*, vol. 112, no. 19, 2018, Art. no. 191901.

[52] H. Xue et al., "Multitarget wireless power transfer system using metasurface for quasi-bessel beams with large half power beam length," *IEEE Trans. Microw. Theory Techn.*, vol. 70, no. 10, pp. 4449–4462, Oct. 2022, doi: 10.1109/TMTT.2022.3197619.

[53] J. Li, Y. Yuan, Y. Wang, S. Yang, Q. Wu, and K. Zhang, "Generating Bessel beams efficiently in microwave with high transmission metasurfaces," *IEEE Trans. Magn.*, vol. 57, no. 6, Jun. 2021, Art. no. 2500805, doi: 10.1109/TMAG.2021.3054020.

[54] C. Pfeiffer and A. Grbic, "Planar lens antennas of subwavelength thickness: Collimating leaky-waves with metasurfaces," *IEEE Trans. Antennas Propag.*, vol. 63, no. 7, pp. 3248–3253, Jul. 2015, doi: 10.1109/TAP.2015.2422832.

[55] Y. Li, X. Fan, P. Li, and J. Zhao, "Subdiffraction focusing metalens based on the depletion of bessel beams," *IEEE Photon. J.*, vol. 14, no. 1, Feb. 2022, Art no 6512805, doi: 10.1109/JPHOT.2022.3144398.

[56] E. S. G. Rodríguez, M. Machnoor, and G. Lazzi, "On the generation of nondiffracting beams in extremely subwavelength applications," *IEEE Trans. Antennas Propag.*, vol. 65, no. 10, pp. 5228–5237, Oct. 2017, doi: 10.1109/TAP.2017.2734160.

[57] I. Derafshi and N. Komjani, "A new high aperture efficiency transmitarray antenna based on huygens metasurfaces," *IEEE Trans. Antennas Propag.*, vol. 70, no. 7, pp. 5458–5467, Jul. 2022.

[58] Y. Wang, F. Qi, Z. Liu, P. Liu, and W. Li, "Ultrathin and flexible reflective polarization converter based on metasurfaces with overlapped arrays," *IEEE Antennas Wireless Propag. Lett.*, vol. 19, no. 12, pp. 2512–2516, Dec. 2020, doi: 10.1109/LAWP.2020.3037907.

[59] A. Darvish and A. A. Kishk, "Near-field shielding analysis of single-sided flexible metasurface stopband TE: Comparative approach," *IEEE Trans. Antennas Propag.*, vol. 69, no. 1, pp. 239–253, Jan. 2021, doi: 10.1109/TAP.2020.3000530.

[60] S. L. Sokol, Z. A. Colwell, S. K. Kandala, M. F. Imani, and S. -M. Sohn, "Flexible metamaterial wrap for improved head imaging at 3 T MRI with low-cost and easy fabrication method," *IEEE Antennas Wireless Propag. Lett.*, vol. 21, no. 10, pp. 2075–2079, Oct. 2022, doi: 10.1109/LAWP.2022.3190696.

[61] S. Lai et al., "A high-performance ultra-broadband transparent absorber with a patterned ITO metasurface," *IEEE Photon. J.*, vol. 14, no. 3, Jun. 2022, Art. no. 4629107, doi: 10.1109/JPHOT.2022.3171864.

[62] M. Bodehou, C. Craeye, H. Bui-Van, and I. Huynen, "Fourier-Bessel basis functions for the analysis of elliptical domain metasurface antennas," *IEEE Antennas Wireless Propag. Lett.*, vol. 17, no. 4, pp. 675–678, Apr. 2018, doi: 10.1109/LAWP.2018.2811620.

[63] T. Cai, G. -M. Wang, X. -L. Fu, J. -G. Liang, and Y. -Q. Zhuang, "High-efficiency metasurface with polarization-dependent transmission and reflection properties for both reflectarray and transmitarray," *IEEE Trans. Antennas Propag.*, vol. 66, no. 6, pp. 3219–3224, Jun. 2018, doi: 10.1109/TAP.2018.2817285.

[64] L. -Z. Song, P. -Y. Qin, and Y. J. Guo, "A high-efficiency conformal transmitarray antenna employing dual-layer ultrathin Huygens element," *IEEE Trans. Antennas Propag.*, vol. 69, no. 2, pp. 848–858, Feb. 2021, doi: 10.1109/TAP.2020.3016157.

[65] R. R. Wildeboer, P. Southern, and Q. A. Pankhurst, "On the reliable measurement of specific absorption rates and intrinsic loss parameters in magnetic hyperthermia materials," *J. Phys. D: Appl. Phys.*, vol. 47, no. 49, 2014, Art. no. 495003.

[66] F. N. Wilson, F. D. Johnston, F. F. Rosenbaum, and P. S. Barker, "On Einthoven's triangle, the theory of unipolar electrocardiographic leads, and the interpretation of the precordial electrocardiogram," *Ann Arbor, MICH*, p. 137, 1954.

[67] K. -K. Shyu, L. -J. Chiu, P. -L. Lee, T. -H. Tung, and S. -H. Yang, "Detection of breathing and heart rates in UWB radar sensor data using FVPIEF-Based two-layer EEMD," *IEEE Sensors J.*, vol. 19, no. 2, pp. 774–784, Jan. 2019, doi: 10.1109/JSEN.2018.2878607.

[68] M. Malik and A. J. Camm, "Heart rate variability," *Clin. Cardiol.*, vol. 13, no. 8, pp. 570–576, 1990.

[69] C. Fournie, F. Chouchou, G. Dalleau, T. Caderby, Q. Cabrera, and C. Verkindt, "Heart rate variability biofeedback in chronic disease management: A systematic review," *Complement. Therapies Med.*, vol. 60, 2021, Art. no. 102750.

[70] D.P. Francis et al., "Physiological basis of fractal complexity properties of heart rate variability in man," *J. Physiol.*, vol. 542, no. 2, pp. 619–629, 2002.

[71] D. Giavarina, "Understanding bland altman analysis," *Biochemia medica*, vol. 25, no. 2, pp. 141–151, 2015.

[72] T. Pham, Z. J. Lau, S. A. Chen, and D. Makowski, "Heart rate variability in psychology: A review of HRV indices and an analysis tutorial," *Sensors*, vol. 21, no. 12, 2021, Art. no. 3998.

Rifa Atul Izza Asyari (Student Member, IEEE) received the bachelor's degree in electrical engineering from Universitas Islam Indonesia, Yogyakarta, Indonesia, in 2016, and the master's degree in telecommunication engineering from National Sun Yat-Sen University, Kaohsiung, Taiwan, in 2019. He is currently working toward the Ph.D. degree in biomedical engineering with the University of Southern Denmark under the SDU Health Informatics Program,The Maersk Mc-Kinney Moller Institute. He was the recipient of the Best Student Paper Award at the Taiwan Annual Symposium 2020. His research interests include the modeling and design of antennas and metasurfaces for healthcare radar applications and signal processing for vital sign sensors in radar.

Kuan-Yuan Lee (Student Member, IEEE) was born in Tainan, Taiwan, in 1997. He received the B.S.E.E. degree in 2020 from National Sun Yat-sen University (NSYSU), Kaohsiung, Taiwan, where he is currently working toward the M.S. degree in electrical engineering. His research focuses on the biomedical signal processing of the radar systems.

Rezki El Arif (Member, IEEE) was born in Sidoarjo, East Java, Indonesia, in 1992. He received the B.S.E.E. degree from Universitas Brawijaya, Malang, Indonesia, in 2015, the M.S.E.E. degree from the National Sun Yat-sen University, Kaohsiung, Taiwan, and the Ph.D. degree form the Department of Electrical Engineering, National Sun Yat-sen University, in 2023. He is currently an Assistant Professor with the Department of Electrical Engineering, Institut Teknologi Sepuluh Nopember, Surabaya, Indonesia. His current research interests include metamaterial-based antennas and signal processing for wearable vital-sign sensors.

Tzyy-Sheng Jason Horng (Fellow, IEEE) was born in Taichung, Taiwan. He received the B.S.E.E. degree from National Taiwan University, Taipei, Taiwan, in 1985, and the M.S.E.E. and Ph.D. degrees from the University of California at Los Angeles, Los Angeles, CA, USA, in 1990 and 1992, respectively. Since 1992, he has been with the Department of Electrical Engineering, National Sun Yat-sen University, Kaohsiung, Taiwan, where he was the Director of the Telecommunication Research and Development Center from 2003 to 2008, the Director of the Institute of Communications Engineering from 2004 to 2007, and is currently a Chair Professor. He has authored or coauthored more than 250 technical publications in refereed journals and conference proceedings, mostly in IEEE publications. He holds more than 50 worldwide patents. His current research interests include RF system-in-package for wireless communications and Doppler radars for biomedical sensing.

Dr. Horng was the recipient of the 1996 Young Scientist Award from the International Union of Radio Science, 1998 Industry-Education Cooperation Award from the Ministry of Education, Taiwan, 2011 Chair Professorship from the Advanced Semiconductor Engineering, Inc., 2012 Outstanding Research Award from National Sun Yat-sen University, 2015, 2020 Outstanding Research Awards, 2020 Future Technology Award, and the 2020 Most Influential Research Monograph Award from the Ministry of Science and Technology, Taiwan, and the 2023 Outstanding Research Award from Pan Wen Yuan Foundation. He has served on the technical program committees of several international conferences, including the IEEE Region ten International Technical Conference, the IEEE International Workshop on Electrical Design of Advanced Packaging and Systems, IEEE Radio and Wireless Symposium, IEEE International Symposium on Radio-Frequency Integration Technology, the IEEE Electronic Components and Technology Conference, and the Asia Pacific Microwave Conference. He was on the Project Review Board of the Division of Engineering and Technologies at the Ministry of Science and Technology, Taiwan, for more than ten years, where he was the Convener of Communications Engineering Program from 2018 to 2020. He was the Founding Chair of the IEEE MTT-S Tainan Chapter in 2009. He was an Associate Editor for IEEE TRANSACTIONS ON MICROWAVE THEORY AND TECHNIQUES from 2012 to 2015.

Daniel Teichmann (Member, IEEE) received the Dipl.-Ing. and Dr.-Ing. (Ph.D.) degrees in electrical engineering and the Dr. rer. medic. degree in theoretical medicine from RWTH Aachen University, Aachen, Germany, in 2009, 2015, and 2022, respectively. He had his two-year post-doctoral education with the Institute for Medical Engineering and Science, Massachusetts Institute of Technology (MIT), Cambridge, MA, USA. From 2015 to 2020, he was the Head of the Laboratory for Medical Instrumentation, RWTH Aachen University. He is currently a Full Professor and the Head of SDU Health Informatics and Technology, University of Southern Denmark (SDU), Odense, Denmark. He explores methods for sensor and information fusion that allow to setup and tailor specialized medical systems dedicated to specific medical needs. This includes the design, building, and testing of sensor devices as well as modeling and simulation of physiologic mechanisms in relation to hemodynamic signal modulation.